

**Combinatorial screening yields discovery of 29 metal oxide photoanodes for solar fuel generation**

Journal:	<i>Journal of Materials Chemistry A</i>
Manuscript ID	TA-COM-12-2019-013829.R1
Article Type:	Communication
Date Submitted by the Author:	28-Jan-2020
Complete List of Authors:	Zhou, Lan; California Institute of Technology, Joint Center for Artificial Photosynthesis Shinde, Aniketa; California Institute of Technology, Guevarra, Dan; California Institute of Technology Richter, Matthias; California Institute of Technology, Joint Center for Artificial Photosynthesis Stein, Helge; California Institute of Technology, Joint Center for Artificial Photosynthesis Wang, Yu; California Institute of Technology, Joint Center for Artificial Photosynthesis Newhouse, Paul; California Institute of Technology, Persson, Kristin; Lawrence Berkeley National Laboratory, Gregoire, John; California Institute of Technology, Joint Center for Artificial Photosynthesis

## COMMUNICATION

## Combinatorial screening yields discovery of 29 metal oxide photoanodes for solar fuel generation

Received 00th January 20xx,  
Accepted 00th January 20xx

Lan Zhou,<sup>a</sup> Aniketa Shinde,<sup>a</sup> Dan Guevarra,<sup>a</sup> Matthias H. Richter,<sup>a,b</sup> Helge S. Stein,<sup>a</sup> Yu Wang,<sup>a</sup> Paul F. Newhouse,<sup>a</sup> Kristin A. Persson,<sup>c</sup> and John M. Gregoire<sup>a,d\*</sup>

DOI: 10.1039/x0xx00000x

**Combinatorial synthesis combined with high throughput electrochemistry enabled discovery of 29 ternary oxide photoanodes, 15 with visible light response for oxygen evolution.  $\text{Y}_3\text{Fe}_2\text{O}_{12}$  and trigonal  $\text{V}_2\text{CoO}_6$  emerge as particularly promising candidates due to their photorepsonse at sub-2.4 eV illumination.**

Solar fuel generation from  $\text{H}_2\text{O}$ ,  $\text{CO}_2$  and sunlight comprises a promising renewable energy technology whose future proliferation relies on materials advancements, including identification of a photoanode for the oxygen evolution reaction (OER). A water-oxidizing photoanode can be coupled to a (photo)cathode for scalable generation of  $\text{H}_2$  and C-containing fuels.<sup>1</sup> Metal oxides are the most extensively studied class of OER photoanode materials due to the availability of a multitude of metal oxide phases that may stably operate in the oxidative electrochemical environment while converting solar to photoelectrochemical (PEC) energy.<sup>2-4</sup>

In addition to historic efforts in developing the binary oxides  $\alpha\text{-Fe}_2\text{O}_3$ ,  $\text{TiO}_2$  and  $\text{WO}_3$  as solar fuels photoanodes, there have been concerted efforts to both explore modes of optimization and understand limiting factors for ternary oxides, most notably  $\text{BiVO}_4$ <sup>2</sup> and also  $\text{ZnFe}_2\text{O}_4$ ,<sup>5</sup>  $\alpha\text{-SnWO}_4$ ,<sup>6</sup> and copper vanadates.<sup>7</sup> high throughput (HiTp) experimental screening of OER photoanodes, pioneered by Parkinson<sup>8,9</sup> and McFarland<sup>10</sup> and advanced by others,<sup>11-13</sup> has accelerated exploration of photoanode candidates. The HiTp techniques described in the present work were previously deployed under guidance from

first principles density functional theory (DFT) calculations, resulting in the discovery of  $\beta\text{-Mn}_2\text{V}_2\text{O}_7$ <sup>14</sup> followed by 8 additional ternary metal vanadates<sup>15, 16</sup> and 5 additional ternary metal manganates.<sup>17</sup> The present work includes ancillary discoveries from this theory-guided work as well as experimental discoveries from screening of composition spaces selected from literature precedent and/or intuition.

Recent reviews of solar fuels photoanodes have highlighted the dearth of metal oxides that operate over a sizable fraction of the solar spectrum, in particular below 2.4 eV, the photon energy onset for  $\text{BiVO}_4$ .<sup>2-4</sup> Herein we report photoactivity of 29 photoanode phases, 15 of which have visible light response and 5 are particularly promising due to the observation of photocurrent at or below 2.4 eV. The measured photocurrents are for non-optimized thin film samples within combinatorial libraries, motivating further development to achieve efficient utilization of the solar spectrum.

The HiTp experimental methods have been described previously and are further detailed in the SI. Briefly, for a given pair of elements, a compositionally graded film is deposited by co-sputter deposition in 6 mTorr of either Ar or mixed Ar/ $\text{O}_2$ , typically resulting in cation variation from ca. 20% to 80% across a 100 mm diameter Si (with Pt conducting layer) or glass (Pyrex or soda lime glass with  $\text{SnO}_2\text{:F}$  conducting layer) substrate. A series of 10-20 locations along each pseudo-binary composition gradient were chosen for characterization via a range of experimental techniques, each with a measurement spot size near or below 2 mm in diameter. Each of the selected locations comprises a thin film sample with approximately uniform composition, and the series of sample provides a composition grid for property measurements. Automated serial experimentation includes measurement of composition (X-ray fluorescence, XRF), crystal structure (X-ray diffraction, XRD), optical absorption (ultraviolet-visible spectroscopy, UV-vis), and photoelectrochemical activity (toggled illumination scanning droplet cell, SDC). The 1-dimensional composition gradient on a 2-dimensional substrate also provides nominally duplicate samples that can be evaluated for reproducibility and/or under

<sup>a</sup> Joint Center for Artificial Photosynthesis, California Institute of Technology, Pasadena, California 91125, United States.

<sup>b</sup> Division of Chemistry and Chemical Engineering, California Institute of Technology, Pasadena, CA 91125, United States

<sup>c</sup> Joint Center for Artificial Photosynthesis, Lawrence Berkeley National Laboratory, Berkeley, CA 94720, United States; Department of Materials Science and Engineering, University of California, Berkeley, CA 94720, United States; Environmental Energy Technologies Division, Lawrence Berkeley National Laboratory

<sup>d</sup> Division of Engineering and Applied Science, California Institute of Technology, Pasadena, CA 91125, United States

\* gregoire@caltech.edu

Electronic Supplementary Information (ESI) available: additional data tables, figures, and experiment details. See DOI: 10.1039/x0xx00000x

different electrochemical conditions, such as different electrolyte pH.

Mining the photoanode experiments in the materials experiments and analysis database (MEAD)<sup>18</sup> resulted in enumeration of the 29 metal oxide phases in Table 1 (XRD-based phase identification summarized in Fig. S5), which to the best of our knowledge have not been reported as photoanodes. Of these, 27 are ternary metal vanadates or manganates related to the computational screening of Refs. <sup>15, 16</sup> and <sup>17</sup>, which were not identified by these prior efforts due to absence of the phase in the Materials Project, unavailability of a band gap energy, or a calculated decomposition energy beyond the threshold of the respective screening pipeline. We note that this compendium of materials can guide development of a set of necessary and sufficient screening criteria based on computation of various structural, electronic, etc. properties. Of particular importance is characterization of the balance of accurate vs. inexpensive band gap calculations to enable accelerated, accurate screening, which is the topic of ongoing work. The other 2 are YFeO<sub>3</sub>-orth, which is a polytype of the hexagonal structure that was previously reported,<sup>19</sup> and yttrium iron garnet (Y<sub>3</sub>Fe<sub>5</sub>O<sub>12</sub>). The photoanodes in Table 1 are sorted by our assessment of their propensity to be photoactive over the visible spectrum. The highest energy LED where photocurrent was not observed (where applicable) and the lowest energy LED where photocurrent was observed is noted, which places a lower and upper limit, respectively, on the photon energy onset of photocurrent. The upper limit is in the visible range for the first 15 phases, demonstrating their visible light response.

The first 5 photoanodes in Table 1 have some photoresponse at 2.07 eV but sustained photocurrent near or below the detectability limit, indicating that the onset for photocurrent is near this photon energy. Among these, Y<sub>3</sub>Fe<sub>5</sub>O<sub>12</sub> and V<sub>2</sub>CoO<sub>6</sub>-tri<sup>†</sup> are the most photoactive, motivating further exploration of their experimental data in Figs. 1 and 2, respectively. The PEC data for the other 3 phases are provided in Figure S2.

PEC characterization of Y<sub>3</sub>Fe<sub>5</sub>O<sub>12</sub> (Fig. 1) demonstrates photoactivity in pH 10 electrolyte and substantially higher photocurrent in pH 13 electrolyte. This difference in performance with pH may be related to a pH-dependent surface passivation layer or a difference in catalytic activity of the operational surface, although the latter is less likely given the lack of photocurrent transients in pH 10 electrolyte. The presence of current transients in pH 13 electrolyte, especially at potentials below 1 V vs RHE suggest that surface optimization to promote catalytic activity and eliminate surface trap states could further improve both photocurrent and photovoltage. The apparent direct band gap from the direct-allowed Tauc signal is 2.35 eV. The substantial absorption tail, large photocurrent with 2.4 eV light source, and some photoresponse with 2.07 eV illumination suggest the presence of an indirect band gap closer to 2 eV. X-ray photoelectron spectroscopy (XPS, Figure S3) characterization after the pH 13 PEC measurements on Fig. 1 showed a near-surface Y/(Y+Fe) concentration of 0.47, slightly larger than the XRF (bulk) value of 0.33 in the as-synthesized film. Neither Y nor Fe is expected to corrode in strong alkaline electrolytes, and the stable

photocurrent under the short duration measurements of Fig. 1 suggest this phase is an excellent candidate for stable photoanode operation.

PEC characterization of V<sub>2</sub>CoO<sub>6</sub>-tri (Fig. 2) in pH 9 electrolyte includes chopped illumination CA at 1.23 V vs RHE, showing some current transients above the sustained photocurrent and photoreponse down to 2.07 eV. An additional 30 minutes of chopped illumination with the 3.2 eV source indicates excellent stability of visible light photoresponse on this time scale, and the chopped illumination CV shows that the onset of photocurrent is below 0.73 V vs RHE. XPS after PEC experiments (Figure S4) revealed near-surface Co/(Co+V) of 0.44, slightly higher than the XRF (bulk) value of 0.35 in the as-synthesized film. V is susceptible to corrosion, although this relatively minor alteration in near-surface composition, combined with the 30 min PEC stability measurement (Fig. 2a), suggest that the film is well passivated by a Co-rich oxide, similar to the passivation behavior of copper vanadate photoanodes.<sup>20</sup>

To put these 2 phases in the context of visible-active metal oxide photoanodes, we consider the 58 metal oxide phases for which we have observed photoanodic activity in our combinatorial experiments. Fig. 3 shows the 7 metal oxide phases with the highest external quantum efficiency (EQE) at 2.41 eV, which includes 2 discoveries from the present work, discoveries from our previous work,<sup>15, 16, 21</sup> and our reproduction of the previously-reported photoanodes FeBiO<sub>3</sub>.<sup>22</sup> While EQE is amenable to optimization, for example through tailoring carrier transport and catalyst coatings, the photon energy of photocurrent onset is more deeply engrained in the electronic structure of the metal oxide phase. After initial development,<sup>23</sup> years of optimization of BiVO<sub>4</sub> led to a 9-fold increase in external quantum efficiency for above-2.4 eV illumination,<sup>24</sup> whereas attempts to instill lower-energy activity have been relatively unsuccessful. The 7 metal oxide phases in Fig. 1 have higher EQE at 2.4 eV than BiVO<sub>4</sub> in our combinatorial experiments, so analogous improvements to these photoanodes could be particularly impactful due to their utilization of a larger portion of the solar spectrum. The remarkable performance optimization of BiVO<sub>4</sub> is concomitant with development of advanced computational and experimental techniques for understanding photodynamics, limiting aspects of carrier transport, electronic structure of heterogeneous surface layers, etc., as recently reviewed by Yang et al.<sup>25</sup> Models of tandem-absorber photoelectrochemical cells indicate that lowering the photon energy onset for the photoanode from 2.4 eV to 2.07 eV could yield a 2-fold improvement in the solar to fuel conversion efficiency and is critical for achieving solar to fuel conversion efficiency in excess of 15%.<sup>26</sup> Per the “fail quickly” model introduced by Parkinson,<sup>27</sup> advanced characterization techniques should be applied to the materials described herein, which pass the critical criterion of visible light photoactivity but may suffer from other intrinsic properties that are not amenable to optimization via known materials engineering strategies.

## Conclusions

Solar fuels photoanodes pose substantial challenges for materials discovery due to the combined needs of solar absorption, charge carrier separation and transport, oxidative stability, and catalytic activity for the OER. Combinatorial screening in composition spaces related to previous theory predictions as well as the photoanode literature resulted in the discovery of 29 metal oxide photoanodes, 15 with visible light response. This unprecedented success in photoanode discovery broadens the set of candidate materials for optimization and integration studies. The onset of photoactivity of  $V_2CoO_6$ -tri and  $Y_3Fe_5O_{12}$ , as well as 3 addition Y-containing metal oxides, near photon energy 2.07 eV make these phases of particular interest for further study to establish the next generation of metal oxide photoanodes for solar fuels technology.

### Conflicts of interest

There are no conflicts to declare.

### Acknowledgements

This material is based upon work performed by the Joint Center for Artificial Photosynthesis, a DOE Energy Innovation Hub, supported through the Office of Science of the U.S. Department of Energy under Award Number DE-SC0004993. Use of the Stanford Synchrotron Radiation Lightsource, SLAC National Accelerator Laboratory, is supported by the U.S. Department of Energy, Office of Science, Office of Basic Energy Sciences under Contract DE-AC02-76SF00515.

### Notes and references

‡ Formula unit suffixes “hex”, “orth”, and “tri” are used to distinguish polytypes with hexagonal, orthorhombic, and trigonal crystal structures, respectively.

1. K. Sivula and R. van de Krol, *Nat. Rev. Mater.*, 2016, **1**, 15010.
2. F. F. Abdi and S. P. Berglund, *Journal of Physics D: Applied Physics*, 2017, **50**, 193002.
3. S. Chu, W. Li, Y. Yan, T. Hamann, I. Shih, D. Wang and Z. Mi, *Nano Futures*, 2017, **1**, 022001.
4. H. He, A. Liao, W. Guo, W. Luo, Y. Zhou and Z. Zou, *Nano Today*, 2019, DOI: <https://doi.org/10.1016/j.nantod.2019.100763>, 100763.
5. J. H. Kim, Y. J. Jang, S. H. Choi, B. J. Lee, J. H. Kim, Y. B. Park, C.-M. Nam, H. G. Kim and J. S. Lee, *Journal of Materials Chemistry A*, 2018, **6**, 12693-12700.
6. M. Kölbach, I. J. Pereira, K. Harbauer, P. Plate, K. Höflich, S. P. Berglund, D. Friedrich, R. van de Krol and F. F. Abdi, *Chem Mater*, 2018, **30**, 8322-8331.
7. C.-M. Jiang, G. Segev, L. H. Hess, G. Liu, G. Zaboriski, F. M. Toma, J. K. Cooper and I. D. Sharp, *ACS Applied Materials & Interfaces*, 2018, **10**, 10627-10633.
8. M. Woodhouse, G. S. Herman and B. A. Parkinson, *Chem. Mater.*, 2005, **17**, 4318-4324.
9. J. G. Rowley, T. D. Do, D. A. Cleary and B. A. Parkinson, *ACS Applied Materials & Interfaces*, 2014, **6**, 9046-9052.
10. T. F. Jaramillo, S. H. Baeck, A. Kleiman-Shwarsstein, K. S. Choi, G. D. Stucky and E. W. McFarland, *J. Comb. Chem.*, 2005, **7**, 264-271.
11. R. Gutkowsky, C. Khare, F. Conzuelo, Y. U. Kayran, A. Ludwig and W. Schuhmann, *Energ Environ Sci*, 2017, **10**, 1213-1221.
12. R. Meyer, K. Sliozberg, C. Khare, W. Schuhmann and A. Ludwig, *ChemSusChem*, 2015, **8**, 1279-1285.
13. J. W. Lee, H. C. Ye, S. L. Pan and A. J. Bard, *Anal. Chem.*, 2008, **80**, 7445-7450.
14. Q. Yan, G. Li, P. F. Newhouse, J. Yu, K. A. Persson, J. M. Gregoire and J. B. Neaton, *Adv En Mater*, 2015, **5**, 1401840.
15. L. Zhou, Q. Yan, A. Shinde, D. Guevarra, P. F. Newhouse, N. Becerra-Stasiewicz, S. M. Chatman, J. A. Haber, J. B. Neaton and J. M. Gregoire, *Adv. En. Mater.*, 2015, **5**, 1500968.
16. Q. Yan, J. Yu, S. K. Suram, L. Zhou, A. Shinde, P. F. Newhouse, W. Chen, G. Li, K. A. Persson, J. M. Gregoire and J. B. Neaton, *Proc. Natl. Acad. Sci.*, 2017, **114**, 3040-3043.
17. A. Shinde, S. K. Suram, Q. Yan, L. Zhou, A. K. Singh, J. Yu, K. A. Persson, J. B. Neaton and J. M. Gregoire, *ACS Energy Letters*, 2017, DOI: 10.1021/acseenergylett.7b00607, 2307-2312.
18. E. Soedarmadji, H. S. Stein, S. K. Suram, D. Guevarra and J. M. Gregoire, *npj Computational Materials*, 2019, **5**, 79.
19. Y. Guo, N. Zhang, H. Huang, Z. Li and Z. Zou, *RSC Advances*, 2017, **7**, 18418-18420.
20. L. Zhou, Q. Yan, J. Yu, R. J. R. Jones, N. Becerra-Stasiewicz, S. K. Suram, A. Shinde, D. Guevarra, J. B. Neaton, K. A. Persson and J. M. Gregoire, *Phys. Chem. Chem. Phys.*, 2016, **18**, 9349-9352.
21. L. Zhou, A. Shinde, S. K. Suram, H. S. Stein, S. R. Bauers, A. Zakutayev, J. S. DuChene, G. Liu, E. A. Peterson, J. B. Neaton and J. M. Gregoire, *ACS Energy Letters*, 2018, **3**, 2769-2774.
22. X. Y. Chen, T. Yu, F. Gao, H. T. Zhang, L. F. Liu, Y. M. Wang, Z. S. Li, Z. G. Zou and J. M. Liu, *Appl. Phys. Lett.*, 2007, **91**.
23. K. Sayama, A. Nomura, Z. G. Zou, R. Abe, Y. Abe and H. Arakawa, *Chem. Commun.*, 2003, DOI: 10.1039/b310428a, 2908-2909.
24. K. R. Tolod, S. Hernandez and N. Russo, *Catalysts*, 2017, **7**, 13.
25. W. Yang, R. R. Prabhakar, J. Tan, S. D. Tilley and J. Moon, *Chem Soc Rev*, 2019, **48**, 4979-5015.
26. K. T. Fountaine, H. J. Lewerenz and H. A. Atwater, *Nat. Commun.*, 2016, **7**, 13706.
27. K. Skorupska and B. A. Parkinson, in *Photoelectrochemical Solar Fuel Production From Basic Principles to Advanced Devices*, eds. S. Giménez and J. Bisquert, Springer International Publishing, Switzerland, 2016, DOI: 10.1007/978-3-319-29641-8, pp. 427-462.

## COMMUNICATION

Table 1: Summary of 29 photoanodes discovered in the present work. The first 15 are designated as visible light photoanodes, 5 with photocurrent onset near 2.07 and 9 with photocurrent onset between 2.41 and 2.75 eV. The 9 phases with no lower limit for photocurrent onset were measured only with the 3.2 eV LED and may exhibit visible light photoactivity. The DFT band gap energy (typically lower than experiment value) using standard MP settings for structure relaxation and subsequent static calculation is shown where available. The electrolyte pH of the corresponding measurements is noted, and any additional electrolyte pH where photoactivity was observed is noted.

Phase name	mp-id	Limits on photon energy onset of photocurrent (eV)		UV-vis band gap (eV)	Computed band gap (eV)	Electrolyte pH	
		lower limit ( $J = 0$ )	upper limit ( $J > 0$ )			discovery experiments	other pH with photoactivity
$\text{Y}_3\text{Fe}_5\text{O}_{12}$	19648	$\leq 2.07$	2.41		N/A	13	10
$\text{V}_2\text{CoO}_6$ -tri	622217	$\leq 2.07$	2.41		1.58	9	
$\text{YMnO}_3$ -hex	19227	$\leq 2.07$	2.41		N/A	13	10
$\text{YMn}_2\text{O}_5$	542867	$\leq 2.07$	2.41	2.5	1.07	10	
$\text{YFeO}_3$ -orth	24999	2.07	2.41		1.56	13	10
$\text{CaMnO}_3$	19201	2.41	2.75	1.41	N/A	13	10
$\text{V}(\text{Bi}_5\text{O}_8)_5$	none	2.41	2.75		N/A	9	
$\text{Nb}_{10.7}\text{V}_{2.38}\text{O}_{32.7}$	none	2.41	2.75		N/A	9	
$\text{NbVO}_5$	769890	2.41	2.75		1.89	9	
$\text{V}_2\text{Pb}_4\text{O}_9$	647385	2.41	2.75		N/A	9	
$\text{V}_2\text{ZnO}_6$	551601	2.41	2.75		N/A	9	
$\text{V}_{4.51}\text{Pb}_{3.5}\text{O}_{14.75}$	none	2.41	2.75		N/A	9	
$\beta\text{-VAgO}_3$	566337	2.41	2.75		N/A	9	
$\text{V}_2\text{Ag}_{0.33}\text{O}_5$	none	2.41	2.75	2.5	N/A	9	
$\text{Ca}_2\text{MnO}_4$	19050	2.41	2.75	1.79	0.37	10	
$\text{Mn}_7\text{SiO}_{12}$	19650		3.2	1.9	N/A	13	
$\text{YMnO}_3$ -orth	25025		3.2	2.3	0.41	13	10
$\text{Mn}_{(2/3)}\text{Sb}_{(4/3)}\text{O}_4$	763546		3.2		0.0	0	13
$\text{Ca}_2\text{V}_2\text{O}_7$	32434		3.2		3.05	9	
$\text{CaMn}_3\text{O}_6$	566229		3.2		N/A	10	13
$\text{Mg}_6\text{MnO}_8$	19239		3.2		2.29	10	
$\text{SrMn}_3\text{O}_6$	none		3.2		N/A	10	
$\text{MnGeO}_3$	643577		3.2		N/A	13	
$\text{V}_2\text{Bi}_8\text{O}_{17}$	none		3.2		N/A	9	
$\text{V}_2\text{Bi}_{12}\text{O}_{23}$	none	2.75	3.2	2.3	N/A	9	
$\text{TaVO}_5$	32407	2.75	3.2		2.17	9	
$\text{V}_2\text{Pb}_2\text{O}_7$	25796	2.75	3.2		2.87	9	
$\text{V}_2\text{Zn}_4\text{O}_9$	504923	2.75	3.2		2.55	9	
$\text{ZrV}_2\text{O}_7$	565725	2.75	3.2		2.59	9	

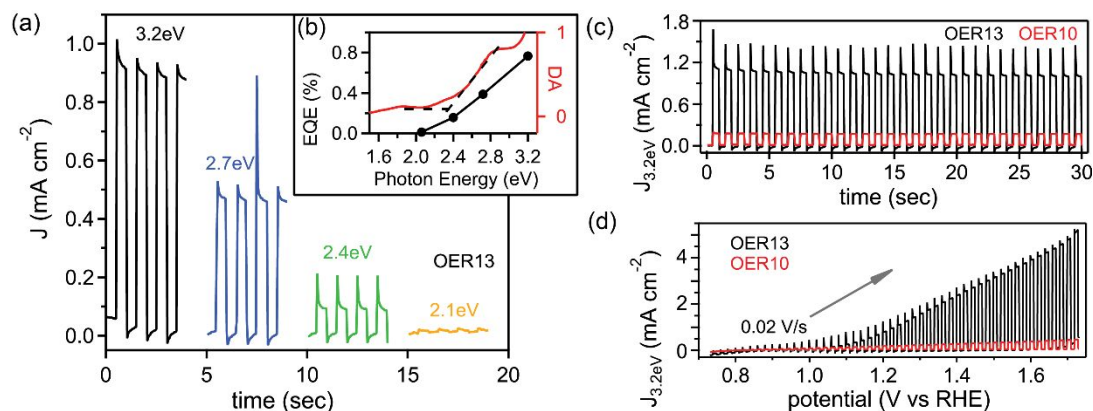


Fig. 1. Summary of toggled illumination PEC experiments on  $\text{Y}_3\text{Fe}_5\text{O}_{12}$  where transition to higher (lower) current corresponds to toggling illumination on (off). (a) CA at 1.23 V vs RHE in pH 13 electrolyte with 4 different light sources. (b) The corresponding spectral EQE (left axis) along with the UV-vis direct-allowed Tauc plot (right axis). Nominally duplicate samples were used to compare activity in pH 10 and pH 13 electrolytes, including (c) 30 s CA at 1.23 V vs RHE and (d) CV with 3.2 eV illumination.

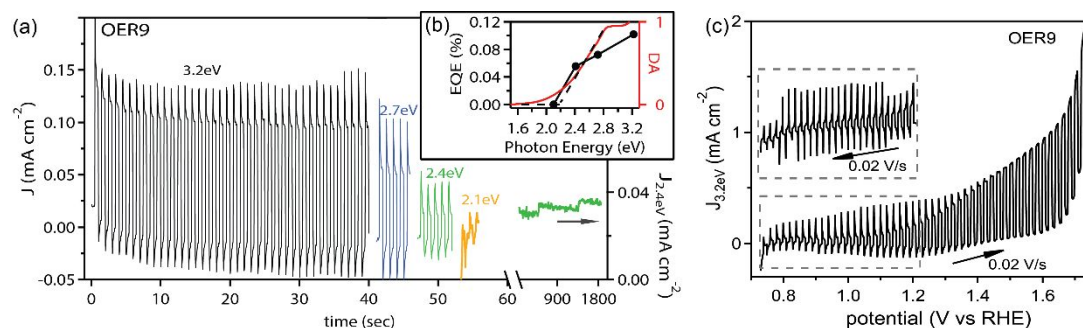


Fig. 2. Summary of toggled illumination PEC experiments on  $\text{V}_2\text{CoO}_6\text{-tri}$  where transition to higher (lower) current corresponds to toggling illumination on (off). (a) CA at 1.23 V vs RHE in pH 9 electrolyte with 4 different light sources (left axis), and an additional 30 min with 2.4 eV illumination where an 11-illumination-cycle moving average of photocurrent is shown (right axis). (b) The corresponding spectral EQE (left axis) along with the UV-vis direct-allowed Tauc plot (right axis). (c) CV with cathodic sweep (inset) starting at 1.23 V vs RHE and anodic sweep extending to 1.73 V vs RHE.

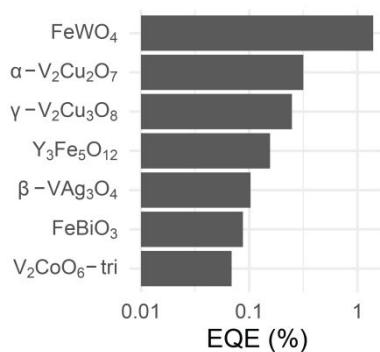


Fig. 3. The top 7 photoanodes by EQE at 2.41 eV from the database of 58 metal oxide photoanode phases (see SI). The photoanodes  $\text{Y}_3\text{Fe}_5\text{O}_{12}$  and  $\text{V}_2\text{CoO}_6\text{-tri}$  reported herein are among the most promising phases due to their visible light photoactivity.